1 # **Supplementary information**

2
3

4 ## **MgO nanocube hydroxylation by nanometric water films**

5

6 *N. Tan Luong, Michael Holmboe, Jean-François Boily[*]*

7

8 Department of Chemistry, Umeå University, SE 901 87 Umeå, Sweden

9

10 ***corresponding author:**
11 **Email:** jean-francois.boily@umu.se
12

Table of Contents

1. Synthesis and Characterization

Two periclase (MgO) samples of contrasting particle size and crystallinity were made by thermal dehydroxylation of synthetic brucite ($Mg(OH)_2$, Fig. S1) at 500 °C (Pe5) and at 1000 °C (Pe10) for 2 h under ambient atmosphere. The resulting periclase powder produced by brucite calcination was cooled down to 25 °C, then stored in a glove box (~18 ppm H_2O) to minimize further exposure to atmospheric moisture and carbon dioxide. The brucite used to produce periclase was originally synthesized by neutralizing of a 0.2 M $MgCl_2$ aqueous solution by a NaOH solution under a flow of $N_2(g)$. It was then repeatedly washed with MilliQ water to remove spectator ions, and dried at room temperature in $N_2(g)$ and stored in a sealed ethylene bottle under ambient condition before the calcination to periclase.

All salient physicochemical properties of Pe5 and Pe10 are reported in Table S1. Phase purity was confirmed by powder X-ray diffraction (XRD) in the 10-90° 2θ range using a PANalytical X'Pert[3] powder diffractometer (1.54187 Å CuKα radiation at 45 kV and 40 mA) operating under reflection mode (Fig. S2).

Particle size and morphology were assessed by Scanning Electron Microscopy (SEM) and bright-field Transmission Electron Microscopy (TEM) imaging. SEM images were taken on a Carl Zeiss Merlin microscope while a FEI Talos L120 microscope (120 kV) was used for low resolution TEM images. High resolution transmission electron microscopy (HRTEM) images were, on the other hand, taken under cryogenic conditions (–90 °C) to minimize the well-known effects of electron beam damage on magnesium hydroxides [1, 2]. These images were acquired with a FEI Titan Krios instrument equipped with field emission gun operated at 300 kV and K2 detector.

Brunauer-Emmet-Teller (BET) specific surface area, Barrett-Joyner-Halenda (BJH) pore size and volume were obtained from 90-point $N_2(g)$ adsorption/desorption isotherms. These isotherms were collected on samples previously degassed at 110 °C under a flow of $N_2(g)$ for 24 h using a Micromeritics TriStar 3000 instrument.

Elemental composition (Table S2) within the top ~10 nm portion of the synthetic Pe5, Pe10, brucite and magnesite particles was identified by X-ray photoelectron spectroscopy (XPS, Kratos Axis Ultra electron spectrometer equipped with Al Kα X-ray source, 150 W, and a delay line detector). Here, survey spectra were collected from 0 to 1100 eV at a pass energy of 160 eV, while core level spectra of C 1s, O 1s and Mg 2p were taken at 20 eV. Water and carbonate surface loadings were, additionally quantified by thermogravimetric analysis (TGA, Mettler Toledo) upon heating from 30 to 700 °C at a rate of 20 °C/min under a flow of $N_2(g)$.

Finally, Temperature Programmed Desorption (TPD) was used to study temperature-induced changes in intersheet hydrogen bonding in brucite. A Pe10 sample reacted under 90 % RH for 5 h was exposed to a heating gradient of 10 °C/min from 40 to 500 °C, during which time vibrational spectral were collected by Fourier-Transformation infrared (FTIR) spectroscopy in transmission mode. Pe10 powder was first pressed onto a fine tungsten mesh (Unique Wire Weaving, 0.002 in. mesh diameter), which was then held by a pierced copper sample holder in direct contact with a K-type thermocouple. The sample holder was placed in the middle of an optical reaction chamber (AABSPEC #2000-A) equipped with CaF_2 windows. The samples were first outgassed for 2 h *in vacuo* (<2.5 mTorr, the detection limit of capacitance manometer; MKS, Baratron), then exposed to 500 mL/min $N_2(g)$-carried D_2O vapor (0.4-70% RH).

2. Characterization results

To study periclase hydroxylation reactions in water films, we compared reaction products from two contrasting types of periclase nanocubes. These were produced by controlled thermal dehydroxylation of synthetic brucite (Figs. S1-S2) [3-5]. Dehydroxylation at 1000 °C produced highly crystalline and monodispersed Pe10 nanocubes (36.7 ± 10.6 nm from imaging; Scherrer crystallite sizes of 31.7 ± 4.2 nm) [6] while dehydroxylation at 500 °C produced considerably smaller Pe5 nanocubes (crystallite sizes of 8.2 ± 0.4 nm) of lower crystallinity (Fig. 2 of main text, Table S1). These Pe5 nanocubes were, additionally, aggregated as nanobars within hexagonal platelets of similar sizes (77 ± 25 nm wide) to those of the brucite nanoparticles from which they formed. Building from the recent discovery[7-9] that water films drive the self-aggregation of periclase nanocubes into nanobars, we infer that transient water films produced during dehydroxylation at 500 °C must have facilitated this aggregation pattern. Aggregated nanobars were also separated by slit-shaped pores likely lying along

97 the (111) plane, producing a maze-like environment.[10, 11] This type of microporosity resulted from the
98 important volumetric compression during hydroxylation, leaving large-scale cracking and voids in
99 platelets of aggregated Pe5 nanocubes (Fig. 2 of main text).[12]

101 This microporosity was confirmed further $N_2(g)$ adsorption/desorption isotherms (Fig. S3).
102 Because specific surface area values ($s_{s,Pe5}$=154 m^2/g, $s_{s,Pe10}$=25.7 m^2/g) were on par with expected
103 values from imaged particles sizes, individual Pe5 and Pe10 nanocube surfaces were accessible for
104 $N_2(g)$ binding. Still, a *t*-plot analysis[13] of these data (Fig. S3) showed that Pe5 contained ~8 times more
105 microporosity (26 μL/g) than Pe10 (3.3 μL/g), in alignment with previous work on controlled
106 dehydroxylation products of brucite.[14] Additionally, because pore size distributions (Fig. S3) were of
107 comparable to Pe5 nanocube sizes, this microporosity must have chiefly arisen from cracks and voids
108 between nanocubes and nanobars, and not within particles. Microporosity in the monodispered Pe10
109 nanocubes must, on the other hand, be chiefly in the form of surface pores.

3. Kinetic modeling

112 Time-resolved Rietveld refinement results of the XRD data (Fig. 3 of main text) were modeled using
113 kinetic growth models from the catalysis literature.[15] Here, the sinusoidal portion of the results up to the
114 first ~10-15 h in both Pe5 and Pe10 were predicting using an Avrami-type[16, 17] nucleation-driven model,
115 and the latter portion in Pe10 using a Shrinking Core Model[18] that accounts for the diffusion-limited
116 transport of reactive species. All calculations were carried out in the computational environment of
117 Matlab 2021b (The Mathworks).

119 The Avrami-Erofeyev[16, 17] model describing the nucleation-limited region accounts for competing
120 ingestion of nucleation sites and of merging nuclei[15] (*cf.* Fig. 1 of main text) with:

122 $$[-\ln(1-\alpha_{AE})]^{1/3}=k_{AE}\,t \qquad\qquad \text{Eq. S1}$$

124 where α_{AE}=[0,1] is the reaction progress, k_{AE} is the Avrami-Erofeyev kinetic constant (h^{-1}) and t is
125 reaction time.

127 The diffusion-limited growth regime was predicted using a 3D diffusion Shrinking Core Model (SCM) to
128 account for the diffusion of reaction species through brucite nanocoatings on MgO. Here, we used the
129 Carter-Valensi[19] adaptation of the Ginstling-Brounshtein model[20]:

131 $$([1 + (z - 1)\alpha_{CV}]^{2/3} + (z - 1)(1 - \alpha_{CV})^{2/3} = z + 2(1 - z)\frac{k_{CV}}{R^2}t \qquad\qquad \text{Eq. S2}$$

133 where α_{CV}=[0,1] is the reaction progress, k_{CV} is the Carter-Valensi kinetic constant (h^{-1}), R is particle
134 radius (nm) and t is reaction time. Of note, this equation applied to spherical particles, which is an
135 reasonable assumption for reacted periclase nanocubes, *i.e.* after dissolution of corners (*cf.* Figs. 5 g-i
136 of main text). Also z in Eq. S2 is the volumetric expansion:

138 $$z = \frac{v_{Mg(OH)_2}}{v_{MgO}} = 1.5 \qquad\qquad \text{Eq. S3}$$

140 where $v_{Mg(OH)_2}$ is the molar volume of $Mg(OH)_2$ and v_{MgO} the molar volume of MgO.

142 Values of t in Eqs. S1 and Eq S2 were solved for preselected values in the α=[0,1] range. The resulting
143 values of α were then solved for experimental values of t. Model predictions were then optimized by a
144 co-optimization of values of k_{AE} and k_{CV} such that

146 $$\alpha_{total} = \alpha_{AE} \cdot f_{AE} + \alpha_{CV} \cdot (1-f_{AE)} \qquad\qquad \text{Eq. S4}$$

148 and where f_{AE} is the fraction of nucleation-limited (Avrami-Erofeyev) contribution to the overall process,
149 such that 1- f_{AE} is the corresponding fraction for diffusion-limited processes. Co-optimization
150 calculations were carried out by minimizing the square of the sum of the deviation of the model to the
151 experimental values of α for a range of predetermined values of f_{AE}. A default values of f_{AE} = 0.5 gave
152 the best-fitting model. At the same time, the trigger time for the diffusion-limited term was optimized to

153   *t*=4 h, and namely where 15 % (α=0.15) of the original periclase underwent conversion. This was
154   procedure was numerically generated using the conditions α_{CV}=0 at *t*=[0,4] h.
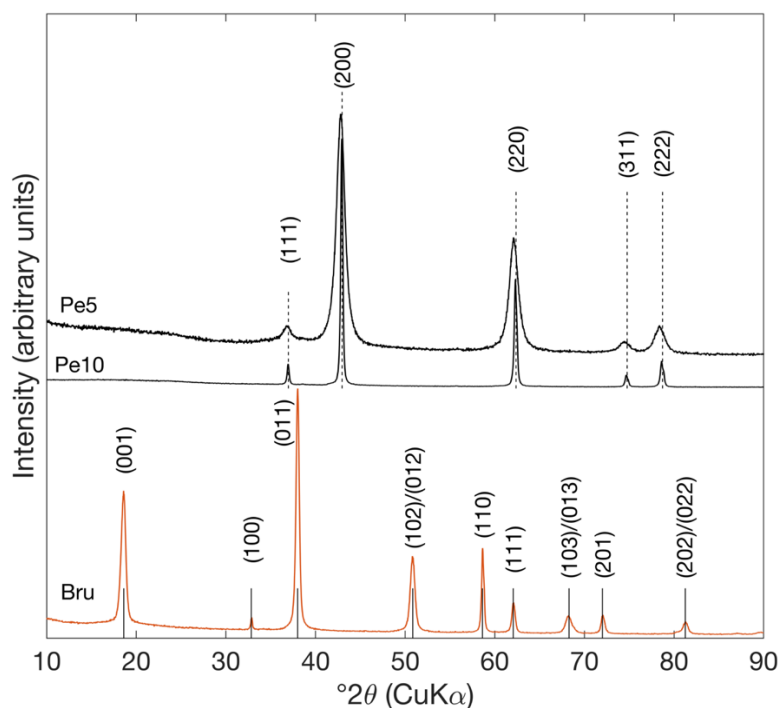155
156
157

158   **Figures**
159
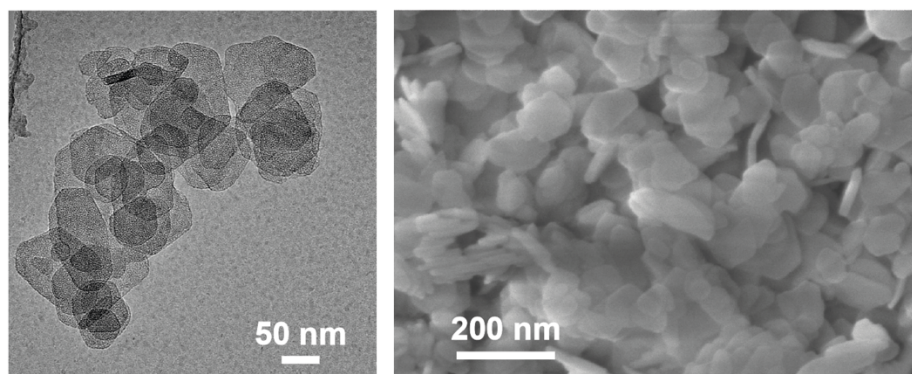
160
161   **Fig. S1.** TEM (left) and SEM (right) of original brucite before dehydroxylation.
162
163
164
165
166
167

168
169   **Fig. S2.** XRD profiles of periclase (Pe5 and Pe10) and brucite (Bru) taken in reflection mode. Reference
170   lines of periclase (dash, AMCSD 0000501)[21, 22] and brucite (solid, AMCSD 0007912)[21, 23] are shown for
171   comparison. Note that the relative intensities of these reference lines were neglected in the plot.
172
173
174
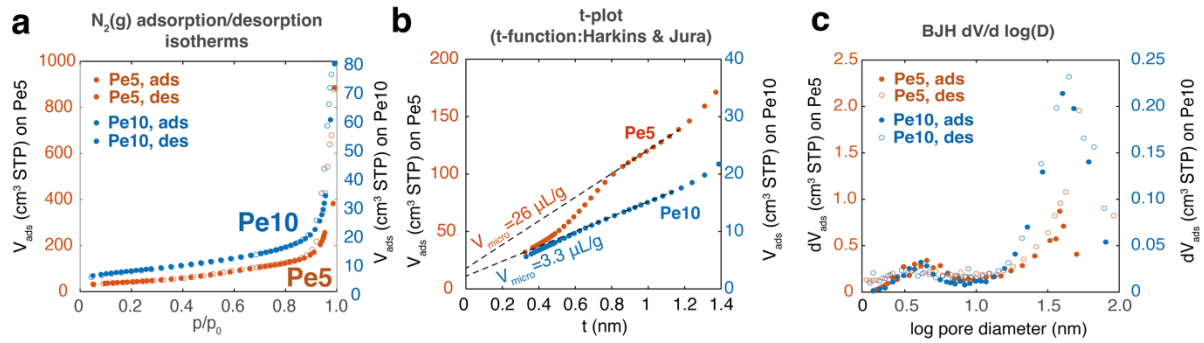
Fig. S3. (a-c) N_2(g) adsorption/desorption isotherm results showing (a) raw data, (b) t-plots and (c) BJH analyses. These revealed specific surface area on par with particle sizes, and microporosity of 26 mL/g in Pe5 but of only 3.3 mL/g Pe10. We assign this microporosity to interparticle voids, given their comparable distributions of values in both Pe5 and Pe10 nanocube assemblages.
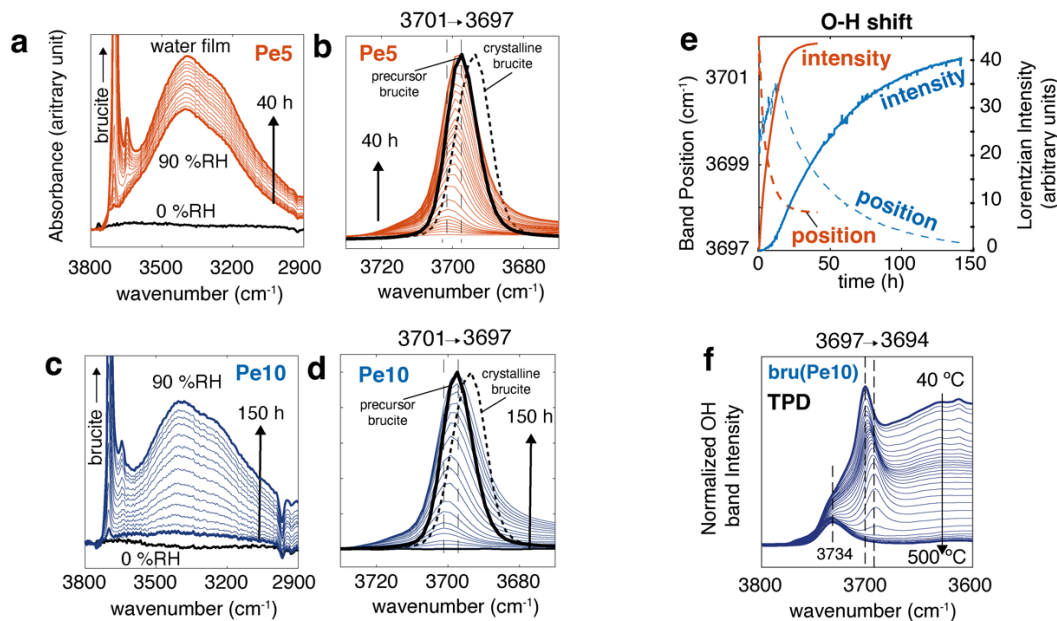

Fig. S4. Hydroxyl group and water film formation, and thermal dehydroxylation of reaction products. (a-d) ATR-FTIR spectra of (a,b) Pe5 and (c,d) Pe10 were exposed to 90% RH over time. Final reaction products have spectral profiles matching that of synthetic brucite (black full lines in b and d) from which Pe5 and Pe10 were made. These were ~3 cm^{-1} blue-shifted in relation to crystalline brucite (dashed lines in b and d), made by aging freshly precipitated brucite at 80 °C for 2 h. Spectra in (b) and (d) were background-subtracted from the data in (a) and (b). (e) The central band position (dashed lines) and intensities (full lines) of the bulk brucite O-H stretching bands, obtained by Lorentzian fitting of the 3680-3720 cm^{-1} region. The band position progressively shifted to that of synthetic brucite particles (black lines in (b) and (d)) from which periclase was originally made. (f) Transmission FTIR spectra of brucite, made by reacting Pe10 at 90% RH for 5 h, during temperature programmed desorption *in vacuo* (40-500 °C, 10 °C/min). O-H stretching bands shifting to the value of crystalline brucite before the onset of dehydroxylation at ~300°C. The resulting periclase was decorated by surface hydroxo groups (3734 cm^{-1}).
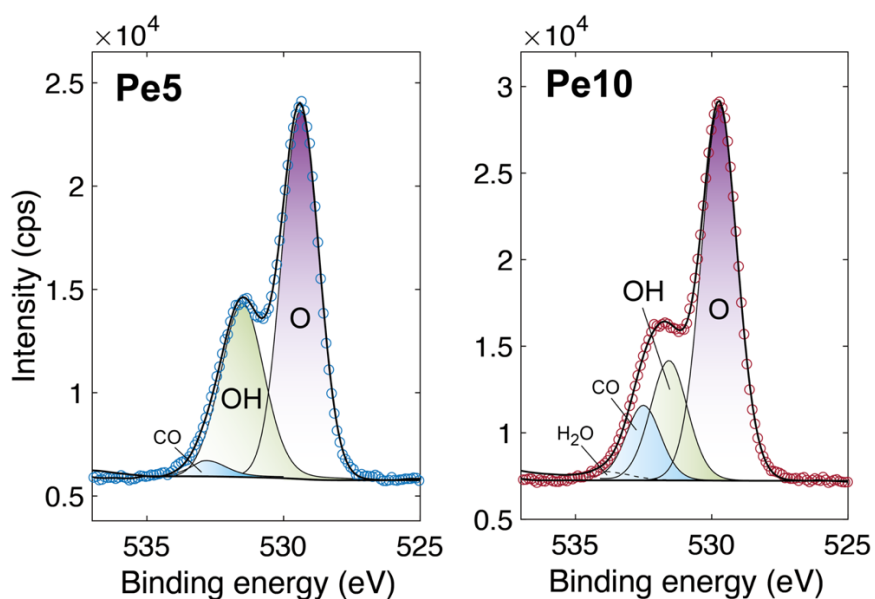
Fig. S5. XPS O 1s spectra of fresh synthetic Pe5 and Pe1 (*cf.* Tables S2-S3). Here, we find that OH groups represent ~$1/4$ of O sites on dry Pe10, and ~$1/3$ of O sites on dry Pe5. Vibrational spectroscopy (Fig. 4) confirmed that these sites were in the form of surface singly-coordinated hydroxo groups at periclase surfaces (–OH or $\equiv$Mg–OH)[24], as can be seen through a narrow band at 3763 cm^{-1}, which is not from bulk brucite (3701 cm^{-1}).

220
221
222
223
224
225
226
227
228
229
230
231
232
233
234
235
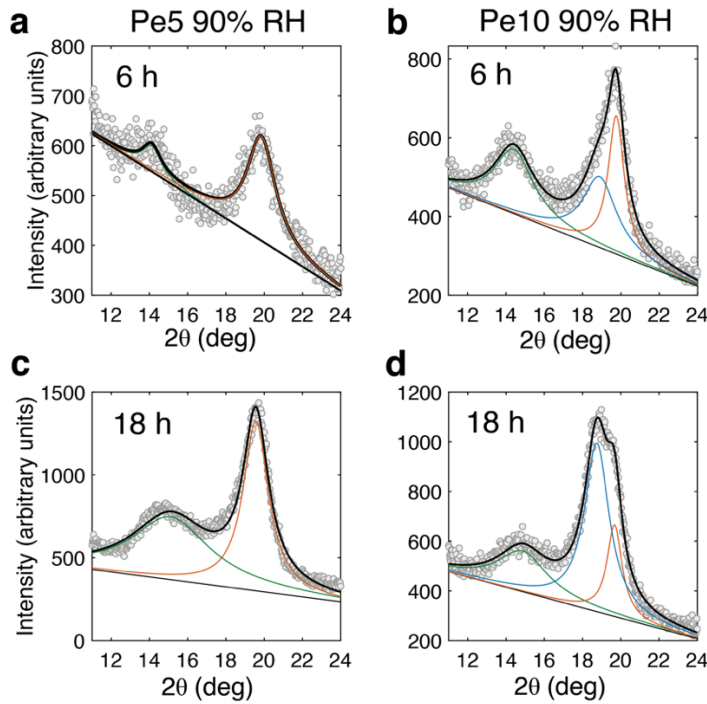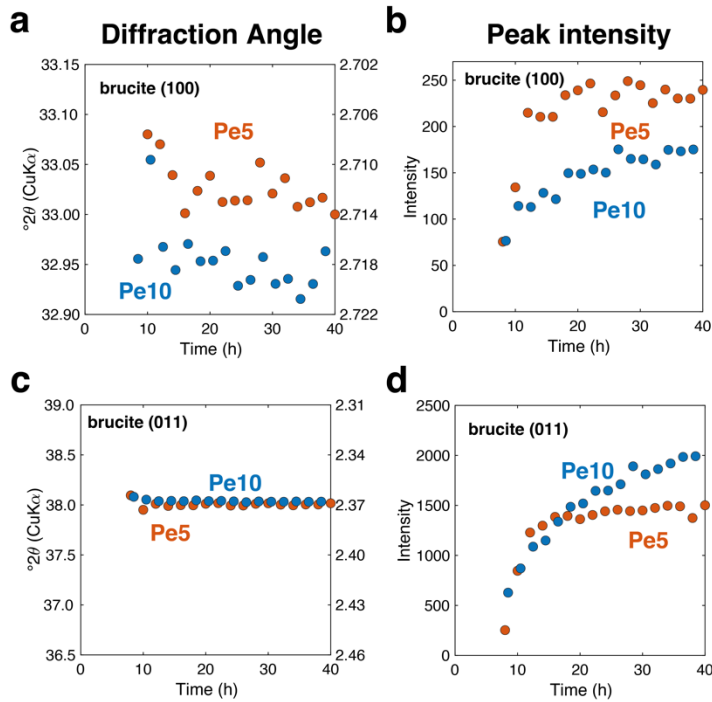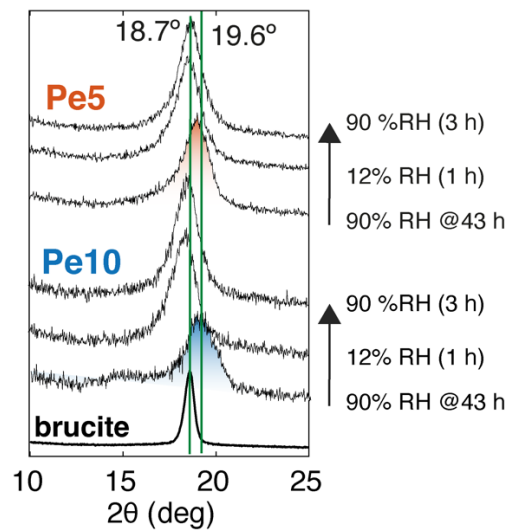236
237
238
239
240
241
242
243
244
245
246
247

Fig. S6. Examples of Lorentzian fitting curves on diffract peaks related to (001) brucite forming on periclase upon exposure to 90% RH.

248
249
250
251
252
253

Figure S7. Periclase and brucite reflections resolved by Lorentzian modeling in Pe5 and Pe10 samples reacted to 90 %RH for up to 40 h.

Fig. S8. (001) reflections of Pe5 and Pe10 after 43 h of exposure to 90 %RH. Dehydration (12 % RH) shifted the 19.6 ° peak back to the 18.7 ° value of brucite. Subsequent rehydration (90 % RH) does not shift the peak back.

Tables

Table S1. Salient physicochemical properties periclase

	Pe5	Pe10
Surface composition[α]	$Mg_{1.00}O_{0.84}(OH)_{0.46}(CO_3)_{0.05}$	$Mg_{1.00}O_{0.89}(OH)_{0.29}(CO_3)_{0.04}$
Particle morphology[β]	hexagonal-like flake	cube
Particle size[β] width (nm)	25-140	17-66
Average (nm)	77 ± 25	36.7 ± 10.6
Crystallite size (nm)[γ]	8.2 ± 0.4	31.7 ± 4.2
Bulk composition[γ]	periclase	periclase
Specific surface area[δ] (m^2/g)	154	25.7

[α] For the top ~10 nm region probed by XPS.
[β] TEM.
[γ] Rietveld refinement of XRD profiles.
[δ] Brunauer-Emmet-Teller (BET) analysis.